Astron. Astrophys. 334, 1085–1094 (1998)

ASTRONOMY AND ASTROPHYSICS

VLBI maps and properties of the 6 GHz OH masers in W 3(OH)

J.F. Desmurs[1,⋆], **A. Baudry**[1], **T.L. Wilson**[2], **R.J. Cohen**[3], **and G. Tofani**[4]

[1] Observatoire de l'Université de Bordeaux 1, BP 89, F-33270 Floirac, France
[2] Max-Planck-Institut für Radioastronomie, Auf dem Hügel 69, D-53121 Bonn, Germany
[3] Nuffield Radio Astronomy Laboratories, Jodrell Bank, Macclesfield, Cheshire, SK11 9DL, UK
[4] Arcetri Observatory, Largo E.Fermi 5, I-50125 Firenze, Italy

Received 23 December 1997 / Accepted 18 March 1998

Abstract. We present the first maps of the ${}^2\Pi_{\frac{3}{2}}, J = \frac{5}{2}, F = 3-3$ and $F = 2-2$ OH maser emission from W3(OH) at 6.035 and 6.031 GHz in both right and left circular polarizations. We used three antennas of the European VLBI Network to achieve a spatial resolution of a few milliarcseconds (mas). Our maps, restored with a beam of 5 x 6.5 mas, show complex OH emission structures in several velocity channels. Weak extended emission structures could be present together with point-like sources. The minimum brightness temperature derived for individual maser spots lies in the range $0.2 - 5\ 10^{10}$ K. The 6.035 GHz maser emission is concentrated in five distinct regions covering the western half of the compact HII region. There are significantly fewer features at 6.031 GHz although the overall spatial distributions of OH features of the $F = 3 - 3$ and $F = 2 - 2$ transitions are similar.

Nearly all OH features with nearby center velocities and opposite senses of circular polarization coincide to within one synthesized beamwidth. We identify these spatially paired components with Zeeman pairs and derive the associated magnetic field strengths, for which some changes have been observed since the first experiment made by Moran et al. (1978). The field always points away from us. The strengths deduced from the 6.035 GHz data range from 2 to 10 mG. At 6.031 GHz the field strengths are also ≤ 10 mG with the exception of a strong feature around -42.6 km s^{-1} which gives ≈ 15 mG. This is the highest field strength measured so far in an OH line.

From our observations we derived the absolute position of the maser emission to an accuracy of order 200 mas for both 6.035 and 6.031 GHz transitions. The fine scale alignment of the $F = 3 - 3$ and $F = 2 - 2$ OH emission maps was made using kinematical and other physical arguments. In the richest area of individual OH spots there is a good match between the strongest 6.035 and 6.031 GHz masers which thus must be excited by similar physical processes. However, the conditions required to excite the 6.031 GHz maser seem to be slightly different from those at 6.035 GHz because the linewidths are narrower and the magnetic fields are stronger at 6.031 GHz.

Send offprint requests to: desmurs@observ.u-bordeaux.fr

⋆ Present address: JIVE / Observatorio Astronómico Nacional, Apartado 1143, E-28800 Alcalá de Henares, Spain

Key words: masers – polarization – ISM: W 3(OH) – radio lines: ISM

1. Introduction

The OH radical is widely distributed in our own Galaxy as well as in several other galaxies. Because of the ubiquity of OH and of its large Lande g factor, measurements of the magnetic field in a variety of objects via the Zeeman effect are possible. Emission from OH is especially strong in the direction of compact HII regions associated with still invisible young massive stars ionizing their immediate surroundings. The evolution of these regions depends on the magnetic field strength, H, whose role is not yet well understood. Therefore, measuring the H field from OH observations provides important information. The right and left circularly (thereafter RCP and LCP) polarized OH spectra observed in the ground-state at 1.6 GHz are often too complex to be interpreted unambiguously in terms of Zeeman pattern. Nevertheless, VLBI observations allow us to identify the polarized features which are spatially coincident, and thus to identify the true Zeeman pairs. This study was successfully undertaken at 1.6 GHz in W3(OH) by García-Barreto et al. (1988) or Bloemhof et al. (1992) and in a number of other sources by Lo et al. (1975) and Hansen & Johnston (1983).

In contrast with the ground state 1.6 GHz emission, the ${}^2\Pi_{\frac{3}{2}}, J = \frac{5}{2}$ state lying immediately above the ground-state exhibits less spectral complexity. The polarized $J = 5/2$ OH emission at 6 GHz should, accordingly, be interpreted in terms of a Zeeman pattern more easily than the 1.6 GHz emission. The two main lines of the $J = 5/2$ state correspond to the hyperfine transitions $F = 3 - 3$ and $F = 2 - 2$ at 6.035 092 and 6.030 747 GHz, respectively. These lines are sensitive to the magnetic field; the Zeeman separation between the RCP and LCP components at 6.035 and 6.031 GHz, is 0.056 and 0.079 km s^{-1} per mG respectively. Thus with a spectral resolution of order 0.1 km s^{-1}, the $J = 5/2$ OH profiles can be measured reliably to detect H field strengths larger than 1 to 2 mG. VLBI observations are of course essential to find the spatially coinciding features with opposite circular polarizations, and thus to identify the true Zeeman pairs.

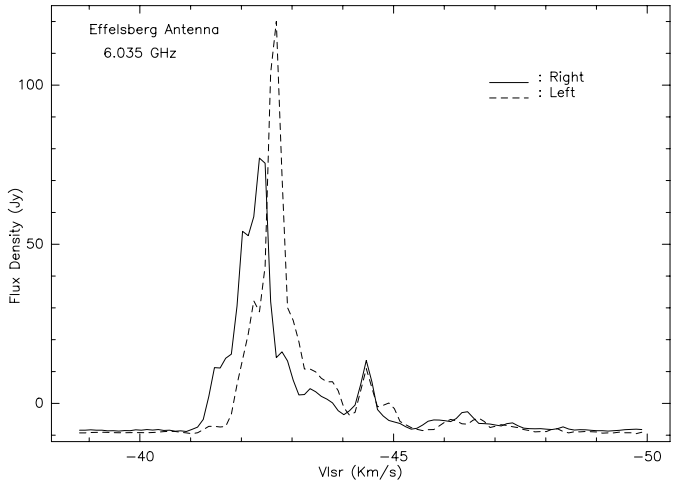

Fig. 1. Effelsberg's auto-correlation spectra of W3(OH) at 6.035 GHz (RCP and LCP) observed in May 1994 with 0.11 km/s resolution.

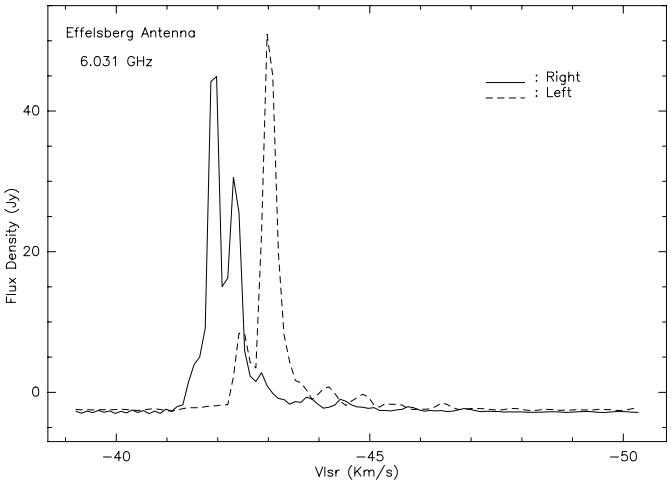

Fig. 2. Effelsberg's auto-correlation spectra of W3(OH) at 6.031 GHz (RCP and LCP) observed in May 1994 with 0.11 km/s resolution.

The VLBI experiment conducted by Moran et al. (1978) (hereafter [Mo78]) showed evidence for the Zeeman effect in the 6.035 GHz OH emission from W3(OH). However, this experiment was never repeated, and the 6.031 GHz line was never observed using VLBI. Apart from W3(OH), several other HII regions are potentially good candidates for 6 GHz OH VLBI observations; such observations could also be used to evaluate the role of the magnetic field in star-forming regions. With these goals in mind we have observed the two main lines of the $J = 5/2$ state in a few HII regions with three antennas of the European VLBI Network (EVN). We report here on the observations made toward W3(OH). In Sect. 2 we give details of our observations and data reduction. In Sect. 3 we present channel maps of the 6 GHz OH sources, and we derive the absolute position of the OH masers. In Sect. 4 we discuss the morphology of the emission and the relative excitation of the two $J = 5/2$ main lines, and we estimate physical parameters of the 6 GHz OH masers. In addition, the H field strength across W3(OH) and some polarization properties are also discussed in Sect. 4. Finally, some conclusions are presented in Sect. 5.

2. Observations and data reduction

The observations were made on May 20 to 23, 1994 using three antennas of the EVN, Effelsberg, Jodrell-MkII (25-m) and Medicina. The total observing time was 48 hours. These antennas provided sensitivities of 1.45, 0.07 and 0.16 K/Jy, respectively. The data were recorded at each station with MKIII terminals in dual circular polarization over a bandwidth of 250 kHz centered on $V_{LSR} = -44$ km s^{-1}, assuming a rest frequency of 6.030 747 and 6.035 092 GHz for the $J = 5/2, F = 2 - 2$ and $3 - 3$ transitions, respectively. Both main lines were recorded simultaneously (in both polarizations) using mode C of the MKIII terminals. For both polarization channels, the system temperatures were around 60 K at Effelsberg (cooled HEMT dual-channel receiver) and 120 K for the two other antennas (uncooled amplifiers).

The total integration time for W3(OH) was 15 hours and we achieved a good uv coverage on source. We also combined observations of the fringe calibrator NRAO150 at regular intervals. Five other HII regions, M17, ON1, W51, NGC7538 and W75N were observed with the same instrumental configuration. These sources were observed during 4 to 7 hours with less uv coverage and lower calibration quality than for W3(OH). Although there is less integrated total flux in these sources (0.2 to 7.5 Jy km s^{-1} in one sense of polarization compared to 70-80 Jy km s^{-1} in W3(OH)), we detected fringes in M17, ON1 and W51; these results will be presented elsewhere. In this paper, we concentrate our discussion on W3(OH) only. A preliminary account of these observations was presented by Desmurs et al. (1997).

The individual telescope outputs were correlated with the Bonn VLBI processor. The averaging time was 10 seconds and the data were later read into AIPS using the task MK3IN. With 112 channels the spectral resolution of the RCP and LCP spectra was 0.11 km s^{-1}. All data were reduced with the NRAO's processing package AIPS installed in the HP workstation of the Observatoire de Bordeaux.

The calibration was obtained from the template spectra method described in Reid (1995). The system temperature and the antenna gain were measured accurately at Effelsberg during the whole EVN session. We integrated the autocorrelated spectra from the 100-m over 30 minutes clear of any problem; these served as our template spectra and are shown for both lines in Fig. 1 and 2. This method is very powerful since it allows us to calibrate the gain of each antenna without knowing all the antenna parameters.

Examination of the visibility plots in our W3(OH) line data base, after fringe calibration on NRAO 150, showed that there was no channel containing a simple point source. Nevertheless, a channel containing a single feature with simple spatial structure and a high S/N ratio can be used as a phase reference for all other channels in order to reduce the fringe residuals in the line database. We used the 6.035 GHz RCP feature lying at -44.5

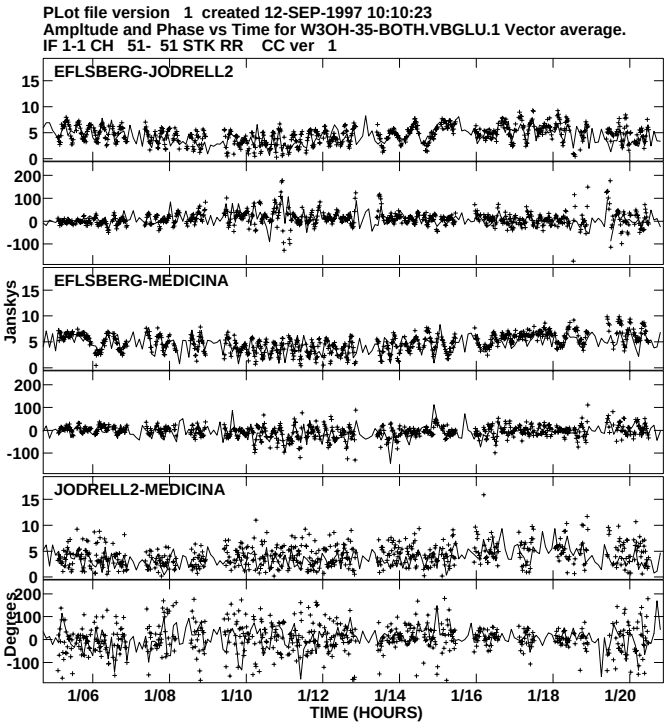

Fig. 3. Visibility plots of the 6.035 GHz RCP reference feature lying at -44.5 km s^{-1}. The continuous line shows the adopted complex gain model.

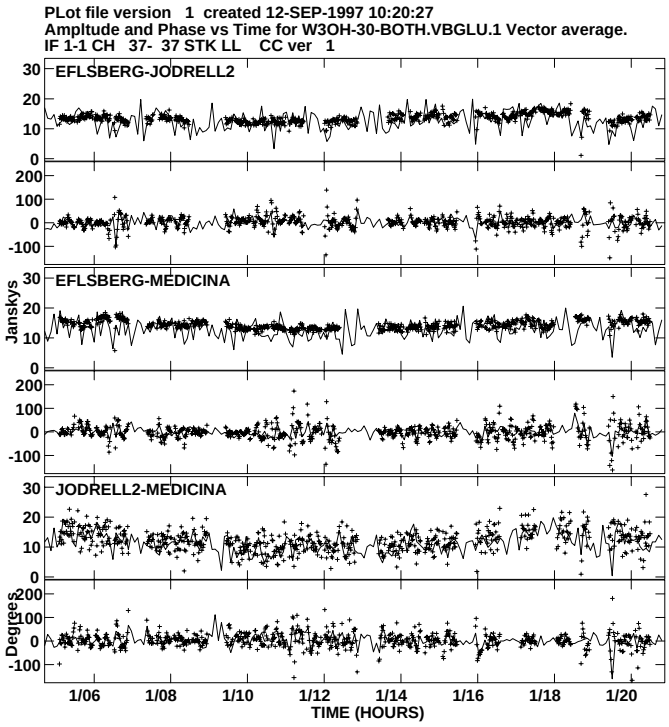

Fig. 4. Visibility plots of the 6.031 GHz LCP reference feature lying at -43.2 km s^{-1}.The continuous line shows the adopted complex gain model.

km s^{-1} as our reference channel. It was selected because: (i) it is not too weak; (ii) it corresponds to a single feature at a given velocity; and (iii) its spatial structure is simple. A similar analysis was applied to the 6.031 GHz line data base with a reference feature at -43.2 km s^{-1}. The visibilities of the two reference features for the three baselines of the array are shown in Fig. 3 (6.035 GHz) and Fig. 4 (6.031 GHz). The fits shown in these figures correspond to the adopted complex gain models. From these plots, the simple structure of the reference channel is clear; the model we used consisted of two simple spots separated by about 5 mas. The model fits the data rather well and in addition we have recovered all the flux density. The complex gain solutions derived from the cleaned maps of the reference features are then applied to all other channels with same polarization and to all other channels with the opposite sense of polarization. This procedure allowed us to accurately localize the LCP and RCP polarized masers without losing any information on the relative positions. In addition, we found that the signal-to-noise ratio in the maps with opposite polarization was improved by selecting a new reference feature in the opposite polarization data base which was: (1) self-calibrated and, (2) used to derive new channel maps. The latter maps cannot be used for relative positions of right and left polarized maser emission, but relative positions can still be obtained from the strongest maser pairs identified in our first step analysis. We note that because the feeds of the alt-az mounted antennas rotate, time varying phase shifts may have been introduced in the LCP data relative to the RCP data. This may partly explain why our self-calibration technique worked better than cross-polarization phase referencing.

In order to localize the areas of OH emission, we have used two different approaches. First, we have summed all OH spectra with velocities between -41.0 and -47.7 km s^{-1} over a 3x3 arc second region centered on the HII region using a modified version of the task AVSPC. Secondly, we have generated with the task MOMNT 2.5 x 2.5 arc second maps for each line channel. Thus we confirmed that all of the emission lies in 5 main regions which we have cleaned more deeply at a later stage. In all cases, the restoring beam was 5x6.5 mas (with a position angle of 45 degrees) and the cell size was 1 mas. For a given sense of polarization and for each line we identify the emission as a real signal on the following basis: (i) emission must be observed at the same position in at least two adjacent channels; (ii) the S/N ratio is at least equal to five with a typical noise threshold of $1\sigma \approx 0.1$ Jy/beam.

Once the regions of OH emission were known, cleaned maps were made with the task IMAGR for all 61 central channels containing the emission. The morphology of the emission and some properties of these maps will be discussed in Sect. 4. The cleaned data cubes were exported in FITS format to the IRAM/Grenoble image analysis package for further analysis with CLASS. The data were first converted into the GILDAS format used by CLASS. Then the data cube was analyzed in velocity. We extracted spectra, along lines of sight separated by 1 mas. Each extracted spectrum was then fitted using a multi Gaussian fit program; we ignored signals lower than 3σ. The results of all fits were stored in a file containing all line parameters. These were used to produce maps integrated in velocity; from these maps are derived accurate positions of the masers, their

peak flux densities, center velocities and linewidths. A more detailed description of the data analysis is given in Desmurs (1996).

3. Results

3.1. Regions of OH emission

Parameters of the maser features, identified as described at the end of Sect. 2, are given in Tables 1 and 2. In Figs. 5 and 6, we show the relative positions of the OH maser spots across W3(OH) for both $J = 5/2$ main lines. At 6.035 GHz there are 5 main regions of OH emission labeled region 1 to 5 on Fig. 5 and in Table 1 and one additional component labeled T. Only regions 1, 3 and 4 contain 6.031 GHz maser features (Fig. 6, Table 2). The velocity intervals are roughly $-47.8 \rightarrow -41.0$, $-44.7 \rightarrow -42.1$, $-43.7 \rightarrow -42.1$, $-43.3 \rightarrow -42.0$ and $-47.0 \rightarrow -46.5$ km s^{-1} for regions 1 to 5, respectively. At 6.035 GHz the overall extent of the emission is $(\Delta\alpha)*cos(\delta) \approx 0.47$ arcsec and $\Delta\delta \approx 2.1$ arcsec. Regions 1 and 3 contain more features than regions 2, 4 and 5. Region 1 is also the richest at 6.031 GHz. An enlargement of region 1 showing 6.035 GHz features in the range -41 to -48 km s^{-1} is presented in Fig. 10. We find a smooth trend in velocity. (Velocities plotted on this figure are the mean velocities of the Zeeman pairs.) Within region 1 there is a general tendency for the velocity to increase from the North to the South. At the the top of this region, we find the most negative velocity (~ -47 km s^{-1}) and we can deduce a gradient to reach ~ -42 km s^{-1} to the South. There is a clear trend in the upper part of region 1 with mean velocities from -47.45 to -42.73 km s^{-1}; this corresponds to an apparent gradient of 6.6 10^3 km s^{-1}/pc. Regions 3 and 4 which are much more compact, do not seem to show this kind of behavior.

From the 61 masers that we detected at 6.035 GHz (see Table 1), we were able to associate 56 components with opposite circular polarizations and velocity separations comparable to or larger than the maser linewidths within one beamwidth. We identify these 28 paired components as Zeeman pairs (see Sect. 4.3) whose properties are given in Table 1. The map at 6.031 GHz shows 21 masers and 9 Zeeman pairs (see Table 2). We note that a small percentage of features in Table 1 (8 %) and in Table 2 (14 %) are unmatched. This is briefly discussed in Sect. 4.3.

3.2. Absolute position of OH masers

Absolute positions of the 6 GHz OH masers allow us to compare maps of OH masers taken at different epochs and wavelengths. We first used the fringe rate mapping technique and the task FRMAP to derive the position of the OH emission in the reference channel. Although at 6.035 GHz, this channel is rather simple, the cleaned map shows that it is not an unresolved point source. In addition, we had only three antennas in the array and we could not derive an absolute position of the reference feature with an accuracy better than ≈ 0.5 arcsec. This result is also due to the fact that the residual delay corrections were determined

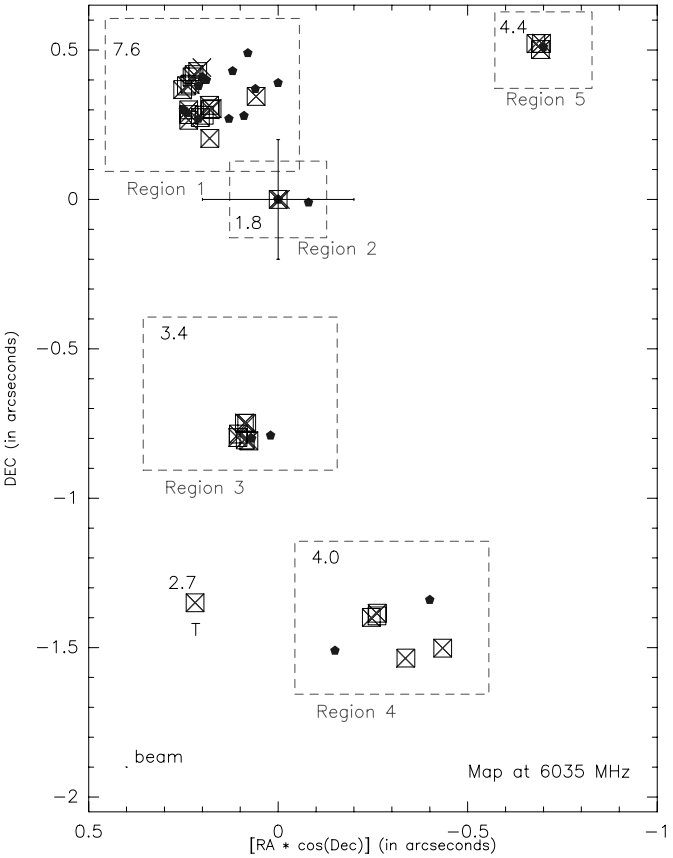

Fig. 5. Map of the relative positions of the 6.035 GHz OH maser features. The RCP and LCP components are shown with crosses $\times$ and open squares $\square$, respectively. The features identified by [Mo78] are shown with stars $\star$. The number in the upper left corner of region 1 to 5 is the magnetic field strength averaged for all individual measurements within each region. The cross at the origin gives the uncertainty in absolute position $\pm 200\ mas$.

from our rather infrequent observations of the fringe calibrator NRAO150. At 6.031 GHz, the spatial structure of the OH features is generally simpler than at 6.035 GHz but the accuracy is not improved.

We then estimated the offset position of NRAO150 from fringe rate maps using delay corrections from the observations of the OH maser which are much more frequent. The RCP feature at -44.5 km s^{-1} and the LCP feature at -44.6 km s^{-1} were used as references at 6.035 GHz. The respective offset positions found were respectively (in mas) : RA$*$cos(Dec) : -168 ± 24 and -141 ± 12 and DEC: -23 ± 24 and -22 ± 25 at -44.5 (RCP) and -44.6 (LCP) km s^{-1}, respectively. We also tried to determined the absolute position by phase referencing NRAO150 to the reference maser. Although the result is consistent with that obtained with FRMAP we have not retained the phase reference solution because NRAO150 is not close to W3(OH). We thus adopt the fringe rate map solution and derive for the 6.035 GHz reference maser at -44.5 km s^{-1} (RCP component lying in region 2 (Table 1, and Fig. 5)): $\alpha(J2000) = 02^h\ 27^m\ 03.^s775 \pm 0.^s03$, $\delta(J2000) = +61^\circ\ 52'\ 24.''96 \pm 0.''2$. A fringe rate map solution was also found for the 6.031 GHz

Table 1. $^2\Pi_{\frac{3}{2}}, J = 5/2$, 6.035 GHz Zeeman pairs in W3(OH) and magnetic field strength. The (0,0) position is in region 2 (see Fig. 5)

Region	Component	Polzn.	$\Delta\Theta_x$ [a] mas	$\Delta\Theta_y$ [a] mas	V_{rad} [b] km s^{-1}	ΔV_{rad} [c] km s^{-1}	S_ν [d] Jy/beam	H [e] mG
2	A	RCP	0	0	-44.50	0.22	4.3	1.8
		LCP	0	0	-44.60	0.19	4.0	
		RCP	-6	-10	-42.20	0.28	2.7	
1	B	RCP	236	300	-41.85	0.25	7.8	9.7
		LCP	236	300	-42.40	0.23	9.6	
		RCP	236	285	-41.60	0.17	4.6	8.9
		LCP	235	284	-41.10	0.17	3.2	
		RCP	236	265	-41.50	0.21	1.2	8.0
		LCP	236	265	-41.95	0.15	2.3	
	C	RCP	241	381	-42.40	0.21	3.0	
		RCP	253	366	-42.70	0.27	1.6	
	D	RCP	181	204	-42.50	0.31	10.5	6.2
		LCP	180	204	-42.85	0.23	22.9	
	E	RCP	206	277	-43.20	0.30	1.3	8.9
		LCP	205	274	-43.70	0.31	1.2	
		LCP	195	282	-43.70	0.22	2.2	
	F	RCP	58	345	-43.10	0.20	3.5	7.1
		LCP	58	345	-43.50	0.17	3.9	
	G	RCP	226	408	-44.30	0.16	2.0	3.6
		LCP	227	410	-44.50	0.19	3.5	
	H	RCP	222	418	-45.90	0.26	1.3	5.3
		LCP	222	418	-46.20	0.32	2.0	
	I	RCP	212	428	-47.20	0.16	0.7	8.9?[f]
		LCP	212	428	-47.70	0.20	0.3?	
	J	RCP	232	385	-44.60	0.18	1.2	6.2
		LCP	233	386	-44.95	0.20	2.3	
	K	RCP	201	441	-47.45	0.21	0.9	
	L	RCP	174	304	-42.20	0.30	26.3	9.8
		LCP	174	304	-42.75	0.26	15.0	
		RCP	180	300	-43.40	0.11	1.9	8.9
		LCP	179	301	-43.90	0.11	0.7	
		RCP	182	315	-44.60	0.26	2.3	7.1
		LCP	181	315	-45.00	0.20	1.1	
3	M	RCP	105	-785	-42.90	0.30	2.5	3.6
		LCP	105	-785	-43.10	0.28	1.4	
		RCP	107	-797	-42.55	0.16	7.9	3.6
		LCP	106	-797	-42.75	0.12	15.8	
		RCP	77	-808	-43.40	0.20	0.8	1.8
		LCP	77	-808	-43.50	0.24	0.7	
	N	RCP	83	-749	-43.55	0.29	3.7	0.9
		LCP	83	-749	-43.60	0.28	5.8	
		RCP	89	-748	-43.10	0.15	1.5	1.8
		LCP	89	-749	-43.20	0.20	1.0	
	O	RCP	80	-804	-42.20	0.29	1.5	8.9?[f]
		LCP	87	-805	-42.70	0.12	1.3	
4	P	RCP	-336	-1536	-42.95	0.12	2.8	4.4
		LCP	-337	-1535	-43.20	0.14	3.4	
	Q	RCP	-261	-1386	-42.95	0.12	1.4	4.4
		LCP	-262	-1385	-43.20	0.18	1.5	
		RCP	-246	-1400	-42.10	0.20	1.0	3.6
		LCP	-246	-1399	-42.30	0.19	1.8	
	R	RCP	-434	-1502	-42.55	0.15	3.4	3.6
		LCP	-434	-1502	-42.75	0.11	3.1	
5	S	RCP	-694	502	-46.60	0.14	0.9	4.4?
		LCP	-692	502	-46.85?	0.12?	0.4	
		RCP	-695	523	-46.55	0.18	0.8	4.4?
		LCP	-695	522	-46.80?	0.20?	0.4	
		RCP	-681	521	-46.60	0.12	0.7	4.4?
		LCP	-680	522	-46.80?	0.12?	0.4	
	T	RCP	219	-1350	-42.10	0.20	3.3	2.7
		LCP	219	-1350	-42.25	0.20	3.4	

Table 1. a) Position offsets were determined as described in Sect. 2. b),c),d) Velocity, FWHM and peak flux determined through Gaussian fitting (see Sect. 2). e) The magnetic field intensity is derived from the velocity difference between the paired RCP and LCP components. f) See text.

reference maser at -43.2 km s^{-1} (LCP component lying in region 1 (Table 2, and Fig. 6)). The absolute position for this maser is : $\alpha(J2000) = 02^h\ 27^m\ 03.^s821 \pm 0.^s03, \delta(J2000) = +61^\circ\ 52'\ 25.^"37 \pm 0.^"2$. The fringe rate map solutions are relatively unstable and we have adopted for the absolute positions, a total error of about ± 200 mas in both right ascension and declination. This is well above our formal errors in the position offsets and conservatively accounts for all uncertainties. The 1950 position found by [Mo78] at 6.035 GHz for their -45.0 km s^{-1} feature transformed into J2000 coordinates is $\alpha(J2000) = 02^h\ 27^m\ 03.^s797 \pm 0.^s03, \delta(J2000) = +61^\circ\ 52'\ 24.^"99 \pm 0.^"2$. Our 6.035 GHz reference feature is close in velocity to the -45.0 km s^{-1} RCP feature observed by [Mo78]. Both positional measurements coincide within the uncertainties.

Table 2. $^2\Pi_{\frac{3}{2}}, J = 5/2$, 6.031 GHz Zeeman pairs in W3(OH) and magnetic field strength. The (0,0) position in this relative map is not that used at 6.035 GHz

Region	Component	Polzn.	$\Delta\Theta_x$ [a] mas	$\Delta\Theta_y$ [a] mas	V_{rad} [b] km s^{-1}	ΔV_{rad} [c] km s^{-1}	S_ν [d] Jy/beam	H [e] mG
1	A'	RCP	0	0	-42.05	0.18	38.4	14.6
		LCP	0	0	-43.20	0.22	17.6	
	B'	RCP	6	-100	-42.40	0.21	8.4	8.9
		LCP	8	-100	-43.10	0.19	12.0	
		RCP	-7	-124	-42.05	0.22	1.4	7.0
		LCP	-8	-124	-42.60	0.19	1.2	
	C'	RCP	63	1	-41.70	0.21	2.6	10.7
		LCP	63	1	-42.55	0.21	3.5	
		LCP	50	-25	-41.90	0.17	0.6	
		RCP	60	-15	-41.50	0.20	0.4?	
	D'	RCP	-116	42	-43.00	0.13	1.6	10.2
		LCP	-116	40	-43.80	0.18	1.3	
	E'	RCP	-8	-96	-41.90	0.20	0.4	7.6
		LCP	-8	-96	-42.50	0.20	0.7	
	F'	RCP	-118	42	-43.00	0.18	1.1	8.9
		LCP	-118	42	-43.70	0.18	1.2	
	G'	LCP	4	63	-42.05	0.18	1.2	
3	H'	RCP	-67	-1101	-42.60	0.15	3.0	5.7
		LCP	-67	-1101	-43.50	0.17	3.9	
4	I'	RCP	-609	-1802	-42.45	0.12	2.7	7.6
		LCP	-609	-1802	-43.05	0.15	2.8	

Table 2. Same footnotes as for Table 1.

Fig. 7 shows our 6.031 and 6.035 GHz reference features against the ionized shell mapped with the VLA around 24 GHz by Baudry and Menten (1995). These strong features lie just on the edge of the northern ionized peak in an area very close to that where the compact $J = 7/2$ OH maser is located (Baudry and Diamond 1998). On the basis of the peculiar $J = 7/2$ emission Baudry and Diamond argued that this area marks perhaps the site of the obscured bright star that excites W3(OH).

Since the absolute positions of the reference features at 6.035 and 6.031 GHz are not known to better than about $\pm$200 mas each, we cannot align the 6.035 and 6.031 GHz maps to better than roughly 300 mas. However, this is sufficient to conclude that region 1 in Tables 1 and 2 is essentially the same for both OH transitions. Our alignment is also consistent with morphological and general arguments deduced from both maps. The area containing the largest number of features in each line is region 1 and the relative distribution of both OH emissions is very similar provided that one superposes the strongest features (see Sect. 4.2). A comparison of velocity dispersions in both OH transitions does not give additional information since velocities ranging from ≈ -41 to -43 km s^{-1} are observed in each region 1 at both 6.031 and 6.035 GHz. Another argument in favour of our proposed alignment is the strength of the magnetic field. The highest values are, in both maps, found in region 1.

4. Discussion

4.1. Morphology of the OH emission and brightness temperatures

Several channel maps exhibit a somewhat extended OH emission structure including the reference channel. In one case, that of component S in region 5 (Table 1), a complex arc-like structure is observed (Fig. 8). However, a spatial resolution higher than that achieved in this work would perhaps reveal more compact structures or a core-halo structure. In several other cases, we have identified masers close in position and velocity and with spatial structure similar to our beamwidth. This is the case of the 6.035 GHz components B and L (region 1) and M (region 3) for which a better spatial resolution would be desirable (see for example map of component B in Fig 9).

In region 1 the 6.031 GHz transition exhibits spatial properties very similar to those at 6.035 GHz, with both point-like and apparently extended emission. In other 6.031 GHz regions the emission is too weak to allow us to detect extended features for which sensitive short baselines are essential.

Our data show that several features have sizes of the order of our beamwidth namely ≈ 5.5 mas. However, we cannot exclude the presence of 5-cm OH sources even more compact than ≈ 5.5 mas, and we thus determine the *minimum* brightness temperature, T_B(K) $\geq 1.5\ 10^9 S$(Jy/beam), where S is the peak flux density in the map. The observed 5-cm peak fluxes range from about 1 to $20 - 40$ Jy/beam corresponding to $T_B \geq 1.5\ 10^9$ K or $\geq 5\ 10^{10}$ K. These limits are well below $T_B \approx 10^{11}$ to 10^{12} K measured in the ground-state (e.g. García-Barreto et al. 1988) or the 10^{11} to 10^{12} K measured at 13.44 GHz by Baudry and Diamond (1998). Since the continuum emission from the HII region is still optically thick around 6 GHz (see flux density spectrum in Baudry et al. 1993) the 6 GHz OH masers must lie in front of the HII region. Therefore, for an unsaturated i.e. purely exponential gain maser amplifying the continuum background we would expect an amplification factor $e^\tau \approx 5\ 10^6$ to reach $T_B = 5\ 10^{10}$ K. In this hypothetical case, the maser gain coefficient for an inverted medium 5 mas long would be $\approx 9\ 10^{-14}$ cm^{-1} at the 2.2 kpc distance of W3(OH). In fact the saturation degree of the maser may be estimated if one knows the maser beam angle, Ω, and the decay rates from the maser levels, Γ. Adopting $\frac{\Omega}{4\pi} \sim 1000$ and $\Gamma \sim 0.15$ s^{-1} the brightness temperature at which the 6 GHz maser becomes saturated is

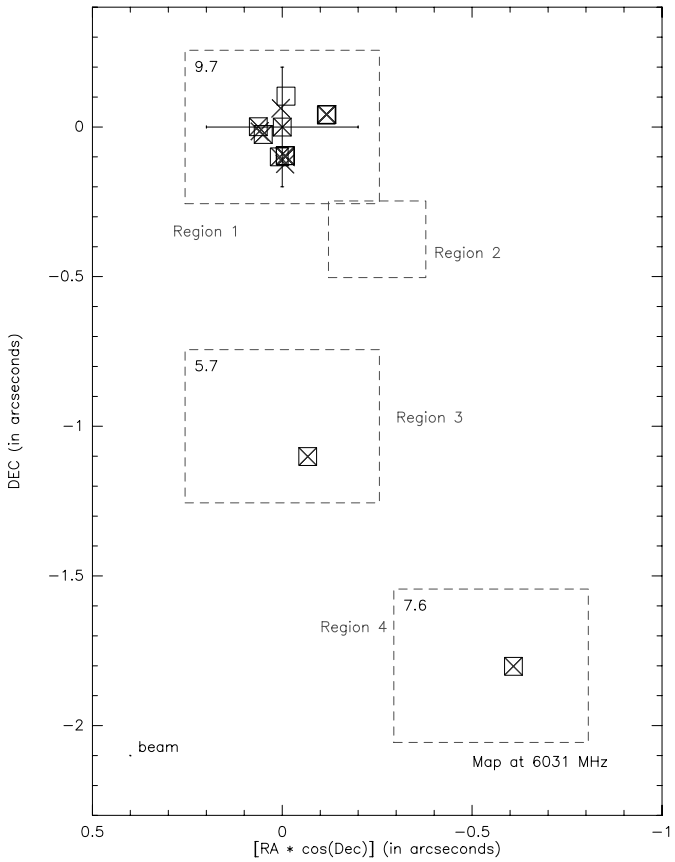

Fig. 6. Map of the relative positions of the 6.031 GHz OH maser features. The RCP and LCP components are shown with stars $\times$ and open squares $\square$, respectively. As for the 6.035 GHz maser the average field strength is given in the upper left corner each box. The cross at the origin, gives the uncertainty in absolute position $\pm 200\ mas$.

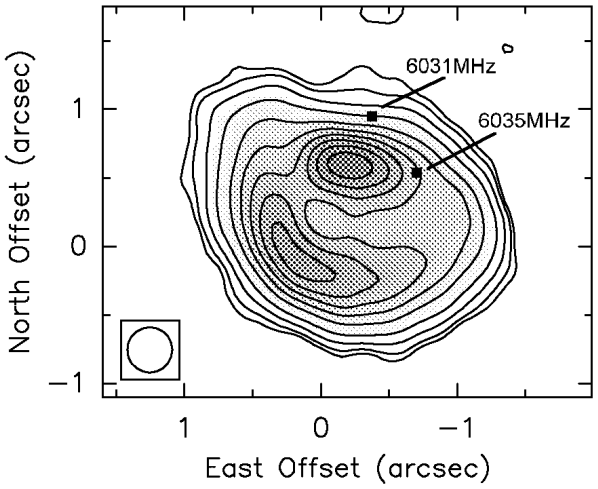

Fig. 7. Positions of the 6.035 GHz and 6.031 GHz reference features superposed on the 23.8 GHz continuum map of the compact HII region mapped by Baudry and Menten (1995).

$T_{sat} \sim 10^{10}$ K. The exact value of T_{sat} is unknown and depends on the pumping routes leading to maser excitation. However, the strongest 6 GHz masers observed here seem to be partially or fully saturated.

4.2. Excitation of the two main lines and variability of the 6.035 GHz maser

As stated previously, the maps of the two main lines can be aligned to about 300 mas. This means that the two regions 1 in both maps are coincident, a fact which is also dictated by arguments based on the spectral complexity of these regions and the matching of velocities across each region (see Sect. 3.2). The agreement in velocity and position is especially good if we superpose the strong 6.031 GHz feature A' at $(-42.05, -43.20)$ km s^{-1} (Table 2) with the strong 6.035 GHz feature L at $(-42.2, -42.75)$ km s^{-1}. Then all of the most Southern features in region 1 tend to coincide in both maps although we cannot make a feature to feature matching. Even the Eastern 6.031 GHz components F', D' can be matched with component F lying more to the West in the 6.035 GHz map. With such an alignment the 6.031 GHz masers in regions 3 and 4 have counterparts in the same regions at 6.035 GHz. Therefore, our results show that both main lines arise in essentially the same gas layers. This is further strengthened by the fact that components A' (6.031 GHz) and L (6.035 GHz) correspond to regions where the magnetic field strength is the highest. Both 6.031 and 6.035 GHz transitions must be pumped by similar processes. However, the 6.031 GHz line is obviously less frequently excited than the 6.035 GHz line although our observations show that in regions of common excitation the brightness temperature may be slightly weaker at 6.035 than at 6.031 GHz. The latter result, if confirmed by future VLBI observations, is surprising and should help to constrain the pumping models of OH.

In addition, differences in the degree of saturation of the two main lines is also suggested by comparing the linewidths. At 6.035 GHz, the linewidths range from 0.17 to 0.32 km s^{-1}, while at 6.031 GHz they range only from 0.15 to 0.22 km s^{-1}. A similar trend was also present in the discrete source survey of Baudry et al (1997). Moreover, the linewidths do not depend on the peak flux density; the largest linewidths are found in some of the weakest and also the strongest feature (e.g. component E and L in Table 1).

Despite probable saturation of the 5-cm OH main lines, variability seems to be present when one compares our 6.035 GHz map with that of [Mo78] made in 1977 April. Such a comparison is meaningful because the absolute position derived in both works is similar within the uncertainties (see Sect. 3.2); it gives us also some insight into the time evolution of the 6.035 GHz maser sources. Both 6.035 GHz maps show reasonable agreement; however, significant differences are noticeable. In particular, [Mo78] observed only one feature in our region 5 and their weak -48.9 and -48.8 km s^{-1} LCP and RCP features were not present in our data. In addition, while the overall spatial distribution of the 6.035 GHz maser has not changed since the epoch of the first map (1997 April), the most powerful maser in the map of [Mo78] would fall in our area 3 where no maser stronger than 5 Jy/beam is detected. This is a clear vari-

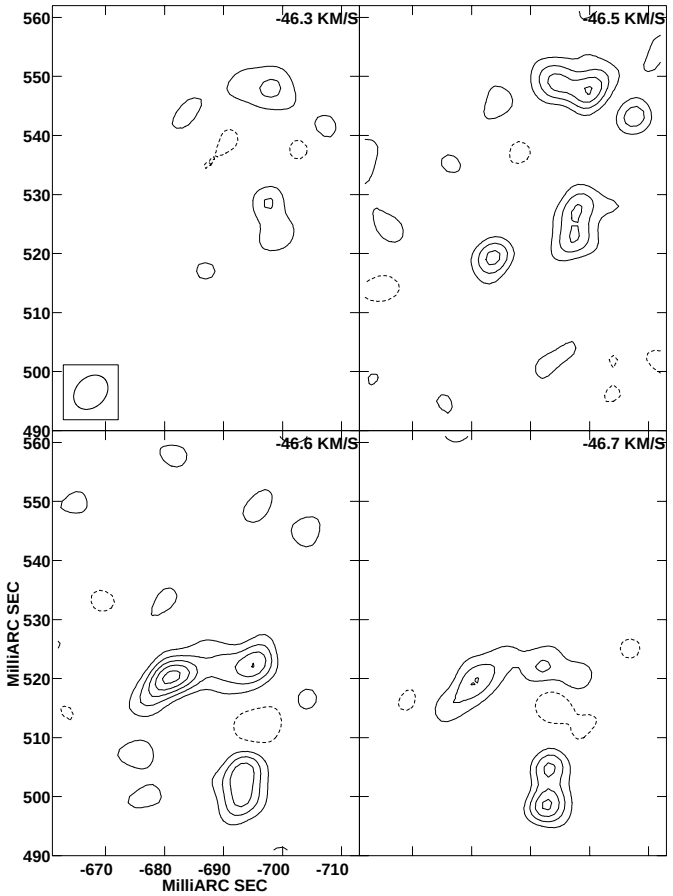

Fig. 8. Apparent arc-like structure of component S at 6.035 GHz (RCP). The contour levels are 0.15 ∗(-1,1,2,3,4,5,6,7,8,9,10) Jy/beam. Positions refer to the map center (in mas).

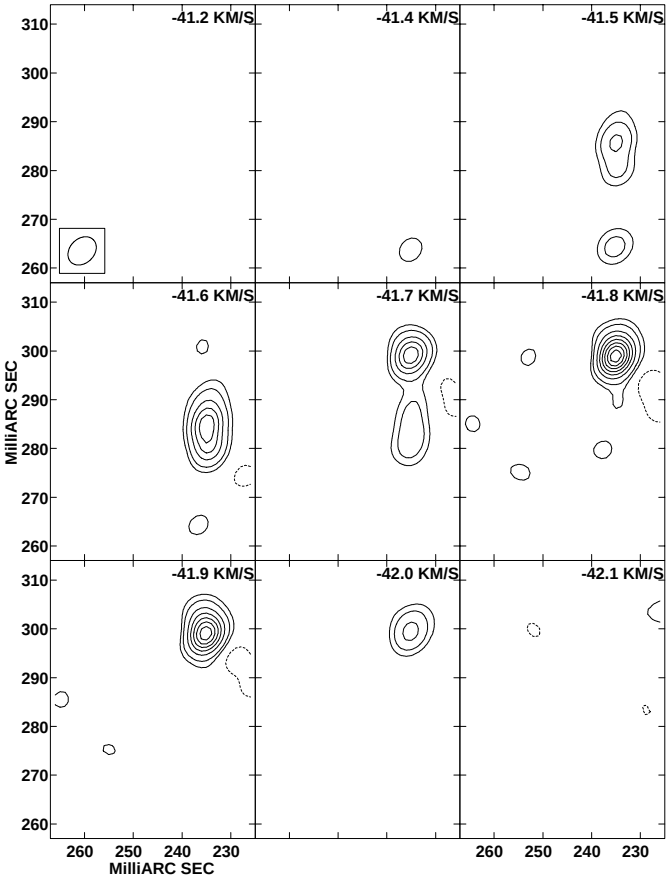

Fig. 9. Example of complex structures in component B at 6.035 GHz (RCP). The contours level are 1.0∗(-0.5, 0.5, 1, 2, 3, 4, 5, 6, 7, 8, 9, 10) Jy/beam.

ation in the intensity of the OH maser. Furthermore, the -48.9 km s^{-1} feature lying to the North East in the map of [Mo78] is not present in our data. Thus we conclude that time variations are possible even for the 6.035 GHz line which one expects to be saturated.

4.3. Magnetic field and polarization properties

Magnetic field strengths estimated from VLBI observations of W3(OH) lie in the range 2 to 11 mG. This is based on observations of the excited-states of OH at 6.035 GHz (Moran et al. 1978 and this work) and 13.44 GHz Baudry and Diamond (1998), and observations of the ground-state at 1665 MHz (García-Barreto et al. 1988, Bloemhof et al. 1992).

The Zeeman effect tends to be weaker for OH states above the ground-state. However, in the $J = 5/2$ state the Landé g-factor is still rather large ($(g_+ + g_-)/2 = 0.485$, Radford 1961). Emission from the hyperfine transitions $J = 5/2, F = 3-3$ and $F = 2-2$ can thus be used to identify Zeeman-split line pairs. In addition, the 6 GHz line profiles are much less complex than in the ground-state and we expect an easier determination of the field strength. In the presence of a magnetic field a single line is decomposed into circularly and linearly polarized $\sigma-$ and $\pi-$components corresponding, respectively, to $\Delta m_F = \pm 1$ and $\Delta m_F = 0$ where m_F is the projection of the total angular momentum on the field axis. If the OH line splitting is greater than or of the order of the maser line widths, the separation between the $\sigma-$components directly gives the total strength of the field. The intensity of these components does not vanish in any direction and reaches a maximum value along the line of sight. Our 6.035 and 6.031 GHz observations show that there are several nearby velocity components with opposite circular polarization which coincide within a fraction of the beamwidth. Such a close spatial relation was not present in the earlier results of [Mo78] who, nevertheless, concluded that there was strong evidence for Zeeman splitting. A high degree of coincidence was also observed in the 13.44 GHz OH pairs identified by Baudry and Diamond (1997). We identify the 6 GHz paired velocity components with $\sigma_\pm$ Zeeman pairs and derive the magnetic field strength from $\Delta V_{\sigma_\pm}$(km s^{-1})/H(mG) ≈ 0.056 and 0.079 at 6.035 and 6.031 GHz.

The Zeeman pairs and field strengths are given in the last column of Tables 1 and 2. The magnetic field derived from the two 5-cm OH main lines in the same area is usually similar with values ranging from about 2 to 10 mG. An exception is the pair A' (Table 2) which shows an unusually strong magnetic field (14.6 mG). Our results for the 6.035 and 6.031 GHz transitions

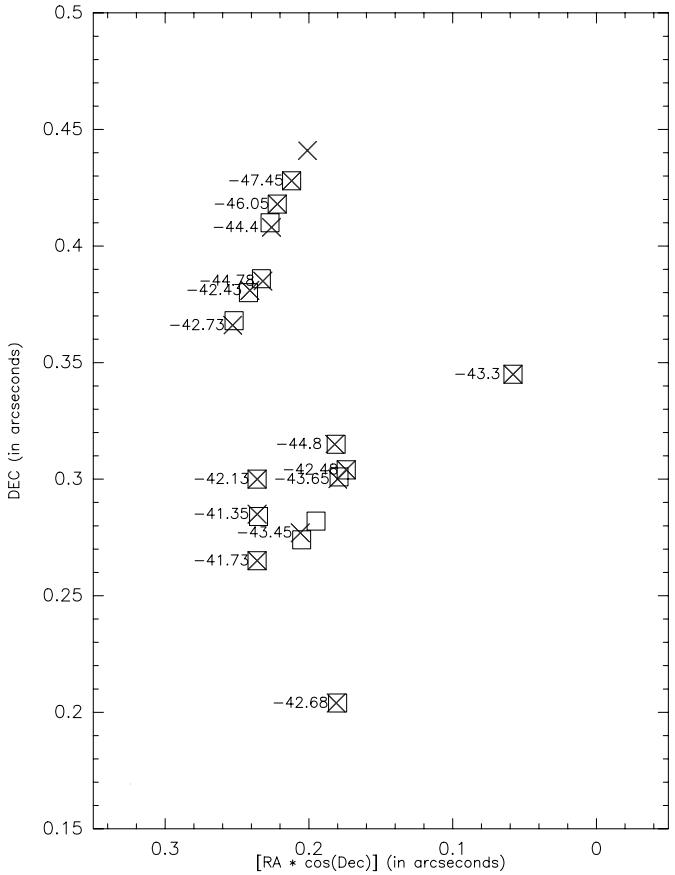

Fig. 10. Mean velocity distribution of identified 6.035 GHz Zeeman pairs in the most complex area (region 1). Crosses and open squares correspond to RCP and LCP components, respectively. This figure is an enlargement of region 1 in Fig. 5.

are consistent with each other and also with values measured by [Mo78]. Note that in Table 1 for pairs I and O we add a question mark to the field strength value. For pair I, the strength seems very different from other pairs in the same region, and the left component is only barely detected. For component O, the two features coincide within 7 mas; this separation is only slightly above our spatial criterion for coincidence. In each region, the variation of the field strength is small. This is especially true in regions showing only a few components; in this case, the measured values vary by only ~ 1 mG. In the complex region 1, the field strength variation is large, ranging from 1 mG to 10 mG (and even 14.6 mG with the Zeeman pair A' at 6.031 GHz). The scatter in the values measured for pairs which are very close in space is small, so that the field strength is consistent. This could be due to local variations of the density. One notes that the values of the field obtained at 6.031 GHz are, generally speaking, greater than those at 6.035 GHz (see average values of the field in the upper left corner of each region in Figs. 5 and 6). This could be an indication that these two masers do not need exactly the same physical conditions; perhaps a slightly higher density is required at 6.031 than at 6.035 GHz although both lines are excited in the same general areas. However, modeling is uncertain and the most recent work of Pavlakis and Kylafis (1996 a,b) which uses recent collisional coefficients does not predict the pumping of the 6 GHz masers accurately since some important coefficients are missing. If the global average value that we found for the field strength is consistent with that of [Mo78], locally we observe great differences. For example in region 4 we find a magnetic field of ~ 4 mG, to be compared to the 9 mG found by [Mo78]. In region 3, we find 2-3 mG, and they found 7 mG. Even for the reference maser which seems to be at the same location in both studies, the values of the magnetic field differ by a factor of 2. In region 1, our range of values is comparable to that of [Mo78] but as the region is complex and shows many features, we cannot conclude that nothing has changed.

Because only the RR and LL intensities were retrieved at the correlation stage, we have no information on the linear polarization. Thus a full polarization analysis of the 6 GHz OH masers is not possible. We note, however, that the percentage of linear polarization is often small at 18 cm ($< 15 - 30\%$) and may even become 0% at 1665 MHz (García-Barreto et al. 1988). In the case of the higher $J = 7/2$, state linear polarization never exceeds 1.5% (Baudry and Diamond 1998). We further note that we have not observed "pure" linearly polarized 5-cm OH features since we do not have in our data RCP and LCP pairs with same velocity. Therefore, it is highly probable that the 6 GHz OH features are fully circularly polarized. The lack of linearly polarized $\pi-$components in their $J = 7/2$ data led Baudry and Diamond (1998) to suggest that the maser radiation propagates essentially along the magnetic field axis and/or that the $\pi-$components are inhibited by some relaxation mechanism during the OH excitation. (The suppression of linear polarization by Faraday rotation is improbable, e.g. García-Barreto et al. 1988). The basic theory of polarized OH masers is given in Goldreich et al. (1973 a, b) and, more recently, in Nedoluha and Watson (1990). These authors showed that the overlap of Zeeman components due to internal velocity gradients give rise to highly circularly polarized OH profiles. Therefore, the circular polarization observed in our data is well explained by the Zeeman effect since one can find matched RCP and LCP components lying in the same regions (Tables 1 and 2).

In some cases, the circularly polarized 6.035 or 6.031 GHz features have no counterpart in the other sense of polarization. This is not due to the weakness of these features but proves that there are no matched Zeeman pairs. This situation is also observed at 18 cm (García-Barreto et al. 1988) and at 13.44 GHz (Baudry and Diamond 1998). It can be understood within the frame of the calculations of Nedoluha and Watson (1990) who propose that the overlap of Zeeman components (due to a velocity difference within the OH cloud exceeding the Zeeman splitting) may enhance one $\sigma-$component.

5. Conclusions

Our 6 GHz observations have opened up a new window for VLBI studies only available with the EVN. With simultaneous observations of two hyperfine transitions, we obtain values of the magnetic field between 2 and 10 mG with a very high confi-

dence since the uncertainty in the spatial coincidence is only a few mas (a few AU at the distance of W3(OH)). The 6.035 and 6.031 GHz masers seem to originate from the same areas but there are some differences which argue for slight different physical conditions; linewidths are narrower and magnetic fields are stronger at 6.031 GHz.

Comparison of our maps with previous observations of the 6.035 GHz line [Mo78] show also that, while the general distribution of the maser groups is preserved over several years, many changes are evident in the major components and in the derived magnetic field strength. Whether this is due to real changes in the emission or to a lack of uv coverage in our VLBI maps is still an open question.

We have also observed some complex structures, in particular an arc like structure at 6.035 GHz, which requires further investigations with more extended VLBI arrays in order to discern extended structures and blended compact components.

Acknowledgements. The authors thank our colleagues who built and installed the 5 cm dual-channel receivers at Jodrell Bank and Medicina. Special thanks go to M. Catarzi (deceased) of the Arcetri Observatory who had the initial responsibility for the 5 cm receiver for Medicina. We especially thank D. Graham who carried out the correlation at the MPIfR. Several colleagues at JIVE and NRAO generously helped us with various tasks in the NRAO's processing system AIPS. J.-F. D. wishes to acknowledge support for this research by the European Union under contract CHGECT920011. Part of this work was supported by the CNRS, URA No. 352 of the Observatoire de Bordeaux. Finally, we wish to thank M.J. Reid for his very useful comments.

References

Baudry A., Desmurs J.F., Wilson T.L., Cohen R.J., 1997, A&A 325, 255
Baudry A., Diamond P.J., 1998, A&A in press
Baudry A., Menten K.M., 1995, A&A 298, 905
Baudry A., Menten K.M., Walmsley C.M., Wilson T.L., 1993, A&A 271, 552
Bloemhof E.E., Reid M.J., Moran J.M., 1992, ApJ 397, 500
Desmurs J.F., 1996, PhD Thesis, Observatoire de Bordeaux, Université Joseph Fourier-Grenoble-I
Desmurs J.F., Baudry A., Graham D., 1997, Vistas in Astronomy Vol 41, No 2, pp 169-173
García-Barreto J.A., Burke B.F., Reid B.F. et al., 1988, ApJ 326, 954
Goldreich P., Keely D.A., Kwan J. 1973 a, ApJ 179, 111
Goldreich P., Keely D.A., Kwan J. 1973 b, ApJ 182, 55
Hansen S.S., Johnston K.J., 1983, ApJ 267, 625
Lo K.Y., Walker R.C., Burke B.F. et al., 1975, ApJ 202, 650
Moran J.M., Reid M.J., Lada C.J. et al., 1978, ApJ 224, L67 [Mo78]
Nedoluha G.E., Watson W.D., 1990, ApJ 361, 653
Pavlakis K.G., Kylafis N.D., 1996a, ApJ 467, 300
Pavlakis K.G., Kylafis N.D., 1996b, ApJ 467, 309
Radford H.E., 1961, Phys. Rev. 122, 114
Reid M.J., 1995, in "Very Long Baseline Interferometry and the VLBA", Chap. 11, ASP conf. ser., vol 82, eds J.A. Zenzus, P.J. Diamond and P.J. Napier